

RE-EXAMINING LARSON'S SCALING RELATIONSHIPS IN GALACTIC MOLECULAR CLOUDS

MARK HEYER¹, COLEMAN KRAWCZYK^{1,2}, JULIA DUVAL³, AND JAMES M. JACKSON³

¹ Department of Astronomy, University of Massachusetts, Amherst, MA 01003-9305, USA; hey@astro.umass.edu

² Department of Physics, Drexel University, Philadelphia, PA 19104, USA

³ Institute for Astrophysical Research, Boston University, Boston, MA 02215, USA

Received 2008 September 8; accepted 2009 May 1; published 2009 June 18

ABSTRACT

The properties of Galactic molecular clouds tabulated by Solomon et al. (SRBY) are re-examined using the Boston University-FCRAO Galactic Ring Survey of $^{13}\text{CO } J = 1-0$ emission. These new data provide a lower opacity tracer of molecular clouds and improved angular and spectral resolution compared with previous surveys of molecular line emission along the Galactic Plane. We calculate giant molecular cloud (GMC) masses within the SRBY cloud boundaries assuming local thermodynamic equilibrium (LTE) conditions throughout the cloud and a constant H_2 to ^{13}CO abundance, while accounting for the variation of the $^{12}\text{C}/^{13}\text{C}$ with galactocentric radius. The LTE-derived masses are typically five times smaller than the SRBY virial masses. The corresponding median mass surface density of molecular hydrogen for this sample is $42 M_{\odot} \text{pc}^{-2}$, which is significantly lower than the value derived by SRBY (median $206 M_{\odot} \text{pc}^{-2}$) that has been widely adopted by most models of cloud evolution and star formation. This discrepancy arises from both the extrapolation by SRBY of velocity dispersion, size, and CO luminosity to the 1 K antenna temperature isophote that likely overestimates the GMC masses and our assumption of constant ^{13}CO abundance over the projected area of each cloud. Owing to the uncertainty of molecular abundances in the envelopes of clouds, the mass surface density of GMCs could be larger than the values derived from our ^{13}CO measurements. From velocity dispersions derived from the ^{13}CO data, we find that the coefficient of the cloud structure functions, $v_{\circ} = \sigma_v/R^{1/2}$, is not constant, as required to satisfy Larson's scaling relationships, but rather systematically varies with the surface density of the cloud as $\sim \Sigma^{0.5}$ as expected for clouds in self-gravitational equilibrium.

Key words: ISM: clouds – ISM: kinematics and dynamics

Online-only material: machine-readable table

1. INTRODUCTION

Giant molecular clouds (GMCs) are the exclusive sites of star formation in galaxies. Their evolution and conversion of interstellar material into stars are governed by the interplay between self-gravity, magnetoturbulent pressure, and feedback processes from newborn stars (McKee 1989). The configuration of a GMC, parameterized by its observed size, velocity dispersion, and mass surface density, offers a snapshot view of its dynamical state. Larson (1981) identified scaling relationships between these observable quantities that have provided the basic, grounding point for all subsequent descriptions of interstellar molecular clouds and star formation. These scaling relationships are: (1) a power law relationships between the velocity dispersion, σ_v , and the spatial scale of the emitting volume, L , $\sigma_v \sim L^{0.38}$, (2) self-gravitational equilibrium, $2\sigma_v L^2/GM \sim 1$, and (3) an inverse relationship between the mean density, n , and size of the cloud, $n \sim L^{-1.1}$. The last of these relationships implies that all molecular clouds have comparable gas surface density. The original compilation of these scaling relationships used molecular line data available from earlier studies. Many of these data were collected with the earliest millimeter wave telescopes and instrumentation and included spatially undersampled maps of molecular line emission from a limited number of nearby (<2.2 kpc) interstellar clouds with poor sensitivity, compared with currently available data.

The Larson scaling relationships have been supplemented with additional observations with improved sensitivity and larger samples. The most significant study to confirm Larson's results is described by Solomon et al. (1987; hereafter SRBY). They used the University of Massachusetts-Stony Brook

(UMSB) Galactic Plane Survey (Sanders et al. 1986) to identify 273 GMCs in the first quadrant. Each cloud was defined as a closed surface within the longitude–latitude–velocity data cube at a given threshold of antenna temperature. For most entries in the catalog, the threshold was 4 K (T_R^*). This high threshold, relative to the noise of the data, was necessary to avoid the blending of emission at lower intensity levels from unrelated clouds that are densely distributed within the $l - b - V_{\text{LSR}}$ domain of the spectroscopic observations. The blending is particularly severe near the tangent points at each Galactic longitude. Realizing that such a high threshold would not fully account for the bulk of the emission from a GMC, SRBY extrapolated the sizes, velocity dispersions, and CO luminosities to the 1 K isophote. After accounting for this low level contribution and its effect on the tabulated properties, SRBY identified a size–line width relationship with a steeper power law relationships index (0.5) than derived by Larson (1981) and concluded that GMCs are self-gravitating objects in virial equilibrium. An algebraic consequence of these two results is that the molecular gas surface density is constant for all clouds with $\Sigma(\text{H}_2) = 200 M_{\odot} \text{pc}^{-2}$. This value is corrected from $170 M_{\odot} \text{pc}^{-2}$ quoted in SRBY to account for the difference in the values adopted for the galactocentric radius of the Sun (10 kpc vs. 8.5 kpc) that affects the virial mass. We have similarly corrected other values in the SRBY catalog (CO luminosity, distance, galactocentric radius, sizes) using the rotation curve of Clemens (1985) with $R_{\odot} = 8.5$ kpc.

The data used by Larson (1981) and SRBY are not optimal for deriving properties of interstellar clouds. In both cases, the observed cloud fields were spatially undersampled with respect to the angular resolution of the telescope used to gather the CO

data. Owing to poor sensitivity or the need for identifying clouds at a high intensity threshold, the target clouds are biased toward the brightest interstellar clouds, the brightest regions within the clouds, or clouds that happen to be nearby or associated with conspicuous star formation. In the case of SRBY, the tracer of molecular gas was $^{12}\text{CO } J = 1-0$ line emission that is optically thick under most prevailing conditions in molecular clouds. Given these limitations, it is reasonable to inquire whether the properties of GMCs and the corresponding Larson scaling relationships can withstand scrutiny with vastly superior data available today. For example, a recent study by Bolatto et al. (2008) examined the properties of resolved GMCs in dwarf galaxies and those within Local Group spiral galaxies. They found the properties of extragalactic GMCs similar to those determined by SRBY for Galactic GMCs.

The Boston University-FCRAO Galactic Ring Survey (GRS) imaged the $^{13}\text{CO } J = 1-0$ emission between Galactic longitudes 18° and 56° and latitudes, $|b| \leq 1^\circ$ with the FCRAO 14 m telescope (Jackson et al. 2006). The advantages of the GRS over the UMSB survey include higher angular sampling and spectral resolution and the use of a mostly optically thin tracer of molecular gas. The lower opacity of ^{13}CO reduces, but does not fully eliminate, the effect of velocity crowding. It also enables a more direct measure of molecular hydrogen column density and mass under the assumption of local thermodynamic equilibrium (LTE; Dickman 1978). These advantages are illustrated in Figure 1, which compares the integrated emission from several clouds identified by SRBY derived from each survey. The UMSB ^{12}CO data identifies the location, angular extent, and velocity of the molecular cloud but is unable to discern any substructure within the cloud. Owing to improved resolution afforded by fully sampling optically thin ^{13}CO emission, the GRS data provide a more precise distribution of molecular material *within* the field with reduced confusion of signal from unrelated clouds along the line of sight. In this study, we examine the properties of the SRBY sample of GMCs using the $^{13}\text{CO } J = 1-0$ data of the GRS.

2. RESULTS

For each GMC entry, the SRBY catalog provides the emission-weighted centroid positions (l_p, b_p, v_p) , angular extents along the Galactic longitude and latitude axes, σ_l, σ_b , velocity dispersion, σ_v , ^{12}CO luminosity, $L_{\text{CO,SRBY}}$, virial mass, $M_{v,\text{SRBY}}$, and near/far side resolved distances, D . Of the 273 GMCs cataloged by SRBY, 180 fall within the coverage of the GRS. All GMC kinematic distances are rederived using the rotation curve of Clemens (1985). However, random motions of clouds with respect to the velocity of the local standard of rest (LSR) and streaming motions owing to spiral arm or localized perturbations introduce errors in such kinematic distances. The fractional error, σ_D/D , can be large for nearby clouds. Over longitudes 20° – 50° and $V_{\text{LSR}} < 20 \text{ km s}^{-1}$, this fractional error ranges from 50% to 200% for velocity dispersions of 10 km s^{-1} . Such errors propagate into significant uncertainties for the derived masses and sizes of the clouds. Therefore, to minimize the fractional error when using kinematic distances, we restrict our analysis to 162 of these GMCs with $V_{\text{LSR}} > 20 \text{ km s}^{-1}$.

A primary goal in this study is to derive the mass and surface density for each cloud over the same area as SRBY. We consider the area, A_1 , defined by the position centroids, l_p, b_p , and the extents, σ_l, σ_b , for each angular axis as listed in the SRBY

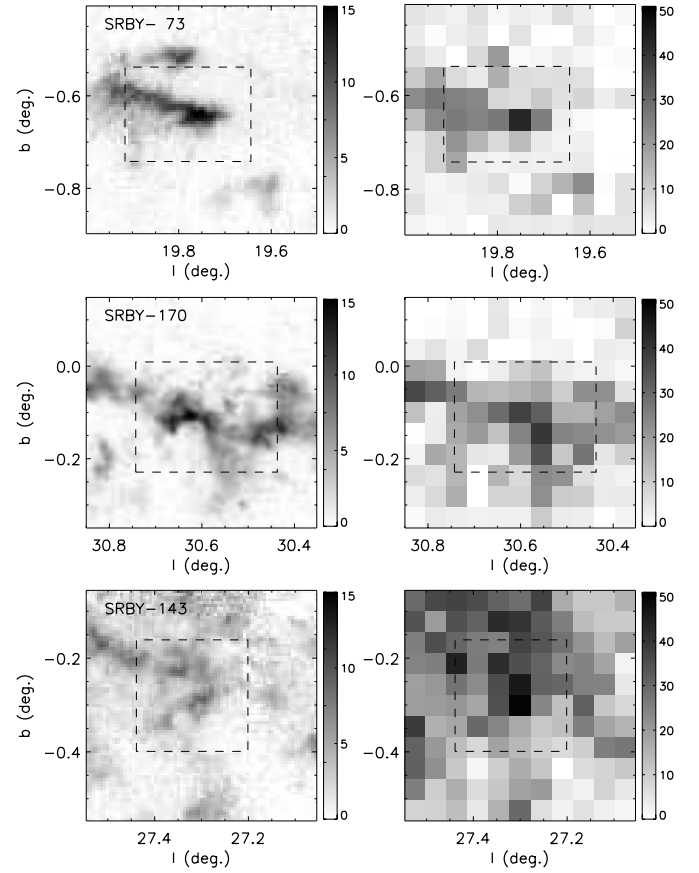


Figure 1. Left: images of integrated $^{13}\text{CO } J = 1-0$ emission from the BU-FCRAO GRS and right: $^{12}\text{CO } J = 1-0$ from the Massachusetts-Stony Brook Survey for three GMCs cataloged by Solomon et al. (1987)—top: SRBY-73; middle: SRBY-170; and bottom: SRBY-143. The densely sampled, lower opacity ^{13}CO line emission offers a more detailed view of cloud structure than is revealed in the undersampled, ^{12}CO data. The dotted lines show the boundary of each cloud based on the emission centroid and angular sizes given by Solomon et al. (1987).

catalog,

$$A_1 = \int_{b_p-1.7\sigma_b}^{b_p+1.7\sigma_b} db \int_{l_p-1.7\sigma_l}^{l_p+1.7\sigma_l} dl \text{ deg}^2, \quad (1)$$

where the factor, 1.7, comes from the relationship between the area of each cloud and σ_l, σ_b described by SRBY. The velocity interval for each cloud is determined from the inspection of the mean ^{13}CO and ^{12}CO spectra over the area, A_1 ,

$$\langle T(v) \rangle = \frac{\int_{A_1} dA T(l, b, v)}{\int_{A_1} dA} \text{ K}. \quad (2)$$

We also derive properties within a secondary area, A_2 , defined as the area within the half-power isophote of the peak column density value within the cloud. Typically, this area is 2%–4% of the SRBY defined area, A_1 , and corresponds to the high column density central core of the cloud.

For each of the 162 clouds within the GRS field and velocity range, the basic properties are re-calculated using the ^{13}CO data, $T(l, b, v)$. The updated properties include emission-weighted centroid positions, l_o, b_o, v_o , and velocity dispersion, σ_v , derived from the second moment of the mean ^{13}CO spectrum of the cloud,

$$\sigma_v^2 = \frac{\sum (T(v))(v - v_o)^2}{\sum (T(v))} \text{ km}^2 \text{ s}^{-2}. \quad (3)$$

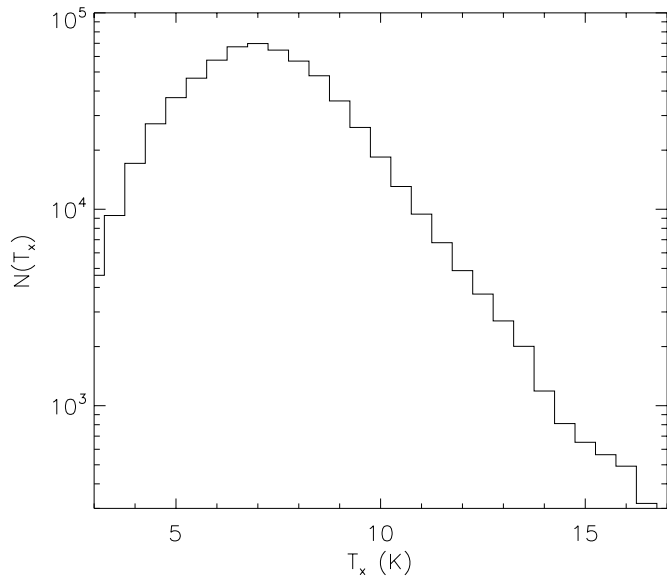


Figure 2. Distribution of excitation temperature values within the SRBY defined areas derived by resampling the UMSB survey onto the GRS grid. The excitation temperatures are smaller than kinetic temperature values expected for GMCs and denote cloud densities less than the critical density of the $^{12}\text{CO } J=1-0$ transition or a filling factor of ^{12}CO emission less than unity over a $45''$ FWHM beam.

The improved angular and spectral sampling of the GRS data provide a more precise position and velocity of the cloud than those provided in the SRBY catalog values. The recomputed values for this sample of clouds are listed in Table 1.

2.1. GMC Masses

The availability of lower opacity $^{13}\text{CO } J=1-0$ emission from the GRS affords a more direct calculation of molecular hydrogen column densities and masses than is provided by ^{12}CO . The ^{13}CO column density is derived assuming LTE conditions within the cloud volume. For each line of sight, l, b ,

$$N_{13}(l, b) = 2.6 \times 10^{14} \left(\frac{\tau_o}{1 - \exp(-\tau_o)} \right) \times \frac{\int T(l, b, v) dv}{(1 - \exp(-5.3/T_x))} \text{cm}^{-2}, \quad (4)$$

where the line center opacity

$$\tau_o = -\ln \left[1 - \frac{T_B}{5.3} ((\exp(5.3/T_x) - 1)^{-1} - 0.16)^{-1} \right] \quad (5)$$

(Rohlfs & Wilson 2003). The excitation temperature, T_x , at each position is determined from the peak temperature of the optically thick ^{12}CO line of UMSB survey data resampled to the GRS grid over the same target velocity interval. The distribution of all spatially resampled T_x values within the area, A_1 is shown in Figure 2. Typical temperatures of GMCs range from 10 to 30 K so the derived excitation temperatures imply either subthermal excitation conditions for most lines of sight or a non-unity filling factor of ^{12}CO emission within the $45''$ beam of the FCRAO telescope.

To relate this column density to the more abundant H_2 component, one requires the abundance ratio of ^{12}CO to ^{13}CO and the ratio of ^{12}CO to H_2 . It has long been established that the ^{12}C to ^{13}C abundance systematically varies with galactocentric

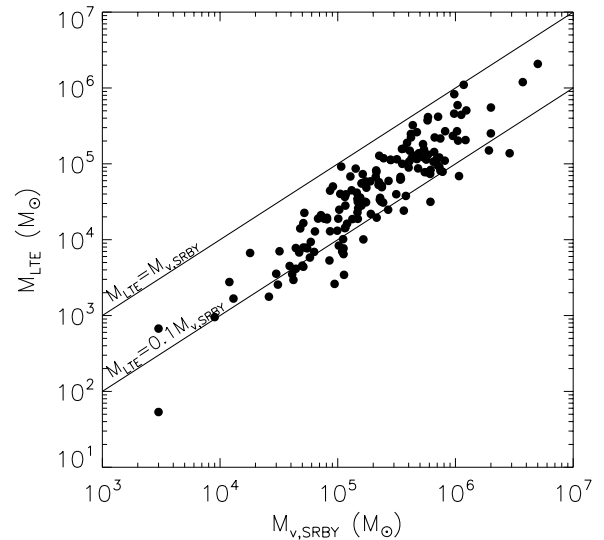


Figure 3. Comparison of cloud masses enclosed within the SRBY defined areas calculated from ^{13}CO assuming LTE, M_{LTE} with virial masses determined by SRBY, $M_{v,\text{SRBY}}$. The LTE masses are systematically lower than the SRBY-derived virial masses.

radius, R_{gal} (Penzias 1980). The most recent characterization of this gradient by Milam et al. (2005) is

$$[^{12}\text{C}/^{13}\text{C}] = 6.2 R_{\text{gal}} + 18.7. \quad (6)$$

This scaling is applied to the ^{13}CO column density for each cloud according to its galactocentric radius, R_{gal} , to derive a ^{12}CO column density, $N_{12}(l, b) = [^{12}\text{C}/^{13}\text{C}] N_{13}(l, b)$. We then derive an H_2 column density, $N_{\text{H}_2}(l, b)$, at each grid position, assuming a constant $\text{H}_2/^{12}\text{CO}$ abundance ratio of 1.1×10^4 (Freking et al. 1982). This value is derived from extinction measurements of the nearby Taurus and ρ Oph clouds and is larger by factors of 2–3 than the abundances determined by Lacy et al. (1994) for lines of sight in the NGC 2024 and NGC 2264 clouds. The adopted abundance values do not account for variations within the cloud owing to photochemistry, fractionation in the outer envelopes, or depletion of carbon onto dust grains in the cold, high-density cores of the cloud. Under these assumptions, the H_2 mass, M_{LTE} , is calculated from integration of the column density distribution, $N_{\text{H}_2}(l, b)$, over the solid angle of each area, A_1 and A_2 ,

$$M_{\text{LTE}} = \mu m_{\text{H}_2} D^2 \int d\Omega N_{\text{H}_2}(l, b), \quad (7)$$

where m_{H_2} is the mass of molecular hydrogen, $\mu = 1.36$, is the mean molecular weight that accounts for the contribution of helium, and D is the distance to the cloud. These masses are listed in Table 1.

A comparison of the virial mass, $M_{v,\text{SRBY}}$, listed in the SRBY catalog, with M_{LTE} within A_1 , is shown in Figure 3. While the values are well correlated, the LTE-derived masses are significantly smaller than the SRBY ^{12}CO virial mass over the same projected area. Typically, $M_{\text{LTE}} \approx M_{v,\text{SRBY}}/5$. One may expect differences in cloud masses, respectively, derived from ^{12}CO and ^{13}CO owing to the relative opacities of the two observed lines and photochemistry so these may not probe equivalent cloud volumes. However, the mass discrepancy illustrated in Figure 3 is larger than differences measured for clouds in the solar neighborhood (Heyer et al. 2006; Goldsmith et al. 2008). In Section 2.3, we discuss the errors and uncertainties associated with each mass estimate.

Table 1
Rederived GMC Properties

SRBY	Within SRBY Defined Area, A_1									Within Half-Max Isophote of $N(\text{H}_2)$, A_2			
	l (deg)	b (deg)	v_o (km s^{-1})	R_g (kpc)	Dist (kpc)	σ_v (km s^{-1})	R (pc)	L_{CO} ($\text{K km s}^{-1} \text{pc}^2$)	M_{LTE} (M_\odot)	σ_v (km s^{-1})	R (pc)	L_{CO} ($\text{K km s}^{-1} \text{pc}^2$)	M_{LTE} (M_\odot)
64	18.87	-0.01	47.6	5.0	12.2	2.6	40.6	1.32e+05	3.23e+05	2.0	5.5	3.46e+03	2.88e+04
67	19.22	-0.23	37.2	6.0	13.3	1.5	42.2	8.27e+04	7.86e+04	1.7	5.0	8.94e+02	4.88e+03
68	19.31	0.03	26.0	6.5	2.2	1.9	6.9	3.91e+03	1.41e+04	2.0	0.8	5.58e+01	8.98e+02
70	19.61	-0.08	60.6	4.7	4.2	3.0	9.7	8.28e+03	1.31e+04	2.6	2.3	4.83e+02	2.74e+03
71	19.63	-0.66	56.7	4.9	4.1	2.2	10.3	8.47e+03	1.89e+04	2.2	3.1	8.70e+02	4.47e+03
72	19.67	0.11	25.0	6.5	13.8	2.4	41.3	1.23e+05	2.61e+05	2.2	9.6	7.17e+03	3.54e+04
73	19.78	-0.64	23.8	6.7	2.0	1.3	4.6	8.42e+02	2.77e+03	0.9	0.5	7.73e+00	6.48e+02
74	19.81	-0.39	68.2	4.3	4.7	2.7	32.1	6.30e+04	1.10e+05	2.3	2.3	4.00e+02	3.50e+03
75	19.90	-0.62	44.1	5.4	3.4	2.8	23.2	5.91e+04	1.28e+05	2.3	1.6	3.39e+02	3.64e+03
77	20.58	-0.42	63.3	4.5	11.3	2.9	33.8	6.20e+04	1.21e+05	2.5	2.9	2.60e+02	9.78e+03
78	20.69	-0.32	62.8	4.7	11.5	1.9	22.8	4.10e+04	7.85e+04	1.7	5.2	3.41e+03	1.95e+04
79	20.76	-0.09	57.8	4.8	11.7	3.1	27.1	9.12e+04	1.89e+05	2.6	4.4	3.29e+03	2.48e+04
80	20.75	0.05	78.2	4.2	5.0	3.1	16.7	1.75e+04	1.95e+04	3.0	4.4	1.98e+03	4.92e+03
81	20.87	-0.02	32.3	6.3	13.5	4.0	45.0	1.41e+05	2.33e+05	3.7	11.7	1.34e+04	4.72e+04
82	20.91	-0.31	66.3	4.5	4.6	1.4	15.3	1.61e+04	1.01e+04	1.5	6.1	2.08e+03	4.63e+03
84	21.54	-0.64	53.5	5.1	3.9	2.0	23.7	3.56e+04	4.92e+04	1.6	0.3	9.61e+00	3.76e+02
85	21.71	-0.02	68.3	4.6	4.5	1.9	18.1	2.31e+04	2.41e+04	2.0	5.3	2.31e+03	6.94e+03
86	21.36	0.00	74.4	4.3	10.9	1.7	32.0	7.85e+04	1.19e+05	1.7	6.7	4.28e+03	1.86e+04
87	21.52	0.26	78.8	4.3	5.0	2.2	7.5	4.24e+03	3.50e+03	2.0	1.8	2.59e+02	6.73e+02
88	21.87	-0.36	82.2	4.2	10.6	2.8	46.0	2.04e+05	2.02e+05	2.5	6.0	3.29e+03	1.54e+04
89	22.07	0.17	51.7	5.3	3.6	2.8	22.9	3.69e+04	6.19e+04	1.8	2.0	4.19e+02	2.62e+03
90	22.34	0.08	84.2	4.1	10.4	1.9	18.4	4.62e+04	5.83e+04	1.8	2.0	3.84e+02	4.51e+03
91	22.41	0.33	84.5	4.1	10.4	1.1	17.1	3.66e+04	4.43e+04	1.2	6.9	3.92e+03	2.82e+04
92	22.54	-0.04	115.1	3.3	7.9	0.5	10.6	1.03e+04	3.44e+03	0.5	1.7	1.16e+02	4.63e+02
93	22.56	-0.20	77.4	4.4	10.8	3.1	11.4	3.32e+04	9.20e+04	3.1	8.8	1.27e+04	6.52e+04
94	22.74	-0.24	106.3	3.4	8.7	2.8	16.0	2.26e+04	5.55e+04	3.2	1.2	1.04e+02	2.32e+03
95	22.81	0.41	91.9	3.9	10.0	2.3	19.8	4.58e+04	3.97e+04	2.5	12.8	1.72e+04	2.92e+04
96	22.86	0.40	114.1	3.3	7.8	2.0	6.4	9.59e+03	5.32e+03	2.1	3.9	1.15e+03	3.47e+03
97	23.00	-0.36	76.6	4.5	10.9	2.3	83.4	1.33e+06	2.08e+06	2.2	5.6	6.26e+03	4.99e+04
98	22.97	-0.02	80.2	4.3	10.6	1.6	28.2	1.47e+05	1.21e+05	1.5	2.2	3.27e+02	4.54e+03
99	23.07	0.64	37.2	6.1	2.8	0.8	8.8	1.60e+03	6.68e+03	0.5	0.6	1.21e+01	7.40e+02
100	23.39	-0.23	99.6	3.7	9.3	4.6	23.3	9.70e+04	4.13e+05	4.1	3.0	2.63e+03	3.22e+04
101	23.51	-0.40	74.9	4.6	4.7	1.5	11.6	1.99e+04	1.45e+04	1.6	5.3	2.50e+03	7.03e+03
102	23.55	0.19	87.3	4.3	10.5	5.9	29.8	1.47e+05	4.18e+05	5.8	12.2	3.84e+04	1.35e+05
103	23.68	0.52	83.2	4.3	5.1	2.0	9.7	4.22e+03	5.81e+03	1.9	2.8	7.86e+02	2.45e+03

Table 1
(Continued)

SRBY	Within SRBY Defined Area, A_1									Within Half-Max Isophote of $N(\text{H}_2)$, A_2			
	l (deg)	b (deg)	v_o (km s^{-1})	R_g (kpc)	Dist (kpc)	σ_v (km s^{-1})	R (pc)	L_{CO} ($\text{K km s}^{-1} \text{pc}^2$)	M_{LTE} (M_\odot)	σ_v (km s^{-1})	R (pc)	L_{CO} ($\text{K km s}^{-1} \text{pc}^2$)	M_{LTE} (M_\odot)
105	23.96	0.14	80.9	4.5	5.0	2.1	8.2	1.12e+04	2.10e+04	2.2	2.2	6.33e+02	4.56e+03
106	24.21	-0.04	88.4	4.2	10.1	1.8	22.7	6.06e+04	8.19e+04	2.1	3.8	1.77e+03	9.05e+03
107	24.45	-0.80	58.4	5.3	3.8	1.6	5.7	3.15e+03	4.55e+03	1.9	3.9	1.35e+03	3.57e+03
109	24.49	0.20	36.4	6.2	12.8	1.7	25.4	3.54e+04	5.27e+04	2.1	7.8	4.99e+03	2.12e+04
110	24.39	-0.24	56.1	5.1	11.5	2.7	19.3	3.62e+04	1.19e+05	2.6	10.5	1.49e+04	6.43e+04
111	24.50	-0.15	44.9	5.9	3.1	1.7	9.7	1.24e+04	2.48e+04	1.9	2.5	7.56e+02	4.02e+03
112	24.42	-0.41	44.3	5.9	3.1	0.9	20.2	2.72e+04	3.77e+04	1.1	0.4	5.76e+00	2.47e+02
113	24.49	-0.72	48.6	5.7	3.2	1.0	9.1	5.09e+03	7.69e+03	1.0	1.2	6.61e+01	6.19e+02
114	24.51	-0.23	96.6	3.9	9.3	2.5	26.4	6.83e+04	1.16e+05	2.5	5.4	4.48e+03	2.06e+04
115	24.54	-0.50	60.6	5.1	4.0	1.9	12.0	1.78e+04	4.17e+04	2.0	5.8	3.30e+03	1.76e+04
116	24.63	-0.14	83.8	4.4	10.3	2.1	25.8	8.20e+04	6.89e+04	2.6	5.8	3.69e+03	1.16e+04
117	24.67	-0.05	110.3	3.5	7.7	3.0	26.3	3.70e+04	1.13e+05	2.1	1.4	1.50e+02	9.43e+03
118	25.18	0.16	103.1	3.8	9.0	3.9	23.3	8.08e+04	1.19e+05	3.4	4.5	2.60e+03	1.32e+04
119	25.27	0.33	45.1	5.8	12.2	1.8	34.7	1.06e+05	9.07e+04	1.3	1.5	8.48e+01	4.16e+03
120	25.54	-0.39	116.3	3.7	7.7	1.8	7.3	3.75e+03	4.40e+03	1.7	3.4	5.34e+02	2.24e+03
121	25.40	-0.24	58.2	5.0	11.2	4.1	52.0	1.58e+05	5.94e+05	3.3	1.4	1.77e+02	4.75e+03
122	25.63	-0.11	94.2	4.2	9.7	2.5	53.7	4.07e+05	5.52e+05	2.2	8.0	7.84e+03	5.20e+04
123	25.54	-0.21	118.1	3.7	7.7	1.7	16.3	1.12e+04	1.87e+04	1.3	1.7	2.07e+02	1.73e+03
124	25.79	0.56	46.3	5.8	3.2	1.8	17.9	1.04e+04	3.16e+04	1.8	6.0	2.22e+03	8.27e+03
125	25.72	0.24	110.7	3.8	8.5	2.0	42.7	1.92e+05	1.50e+05	2.0	5.3	3.82e+03	2.12e+04
126	25.91	0.22	69.6	4.9	4.4	1.3	7.2	4.09e+03	3.55e+03	1.5	2.8	3.33e+02	1.05e+03
127	25.71	-0.15	106.3	3.8	8.5	2.1	34.0	6.78e+04	1.15e+05	2.1	3.7	1.26e+03	4.39e+03
128	25.90	-0.13	104.8	3.9	8.7	2.5	37.4	1.75e+05	2.06e+05	3.1	7.0	4.33e+03	1.68e+04
129	25.96	-0.57	62.0	5.2	4.1	1.4	9.6	4.51e+03	4.14e+03	1.5	3.2	4.26e+02	1.11e+03
130	26.18	0.13	70.5	4.9	4.5	1.5	12.8	7.88e+03	1.02e+04	1.5	5.9	2.05e+03	5.45e+03
131	26.35	0.79	47.1	5.9	3.1	1.2	8.4	2.91e+03	7.04e+03	1.7	0.4	3.28e+00	1.12e+02
133	26.55	-0.31	107.7	3.9	8.5	2.0	16.1	2.59e+04	4.48e+04	1.9	1.8	2.82e+02	3.13e+03
134	26.60	0.01	26.8	7.0	13.4	2.5	25.8	9.47e+04	1.49e+05	2.8	3.6	1.35e+03	1.02e+04
135	26.66	0.01	99.6	4.1	9.1	3.3	38.5	1.40e+05	8.11e+04	3.0	11.4	1.38e+04	1.87e+04
136	26.68	0.52	87.2	4.5	5.2	1.6	12.2	6.62e+03	7.88e+03	1.7	1.6	1.40e+02	9.37e+02
137	26.68	0.01	111.2	3.8	7.6	1.0	12.5	9.75e+03	6.97e+03	1.1	3.3	6.31e+02	2.14e+03
138	26.93	0.13	92.4	4.4	5.5	1.7	16.9	2.38e+04	3.05e+04	1.6	1.8	2.24e+02	1.38e+03
139	27.00	-0.39	68.1	5.0	4.3	1.8	6.1	2.45e+03	2.55e+03	1.8	2.8	5.81e+02	1.34e+03
140	26.90	-0.11	79.8	4.7	5.0	1.6	17.7	9.50e+03	1.42e+04	1.9	3.2	7.61e+02	2.85e+03
141	27.04	-0.15	102.8	4.1	9.0	1.4	14.8	2.18e+04	1.85e+04	1.4	3.0	5.08e+02	2.72e+03
142	27.24	0.14	33.3	6.6	12.9	2.6	29.0	8.54e+04	1.32e+05	2.4	5.1	2.83e+03	2.46e+04
143	27.32	-0.28	74.2	5.0	4.5	3.2	10.5	7.50e+03	6.45e+03	2.6	3.4	8.48e+02	1.81e+03
144	27.35	-0.15	92.4	4.4	5.6	1.6	9.2	1.13e+04	1.66e+04	1.5	1.1	1.26e+02	1.54e+03
145	27.52	0.21	35.4	6.5	12.7	1.0	17.0	2.46e+04	1.88e+04	1.1	2.6	5.75e+02	2.21e+03
146	27.50	0.14	97.5	4.3	9.3	3.6	23.3	8.86e+04	1.55e+05	4.1	10.4	1.78e+04	5.47e+04
147	27.63	0.10	82.9	4.7	5.1	1.5	15.0	1.71e+04	2.19e+04	1.8	0.7	3.15e+01	5.57e+02
148	27.73	0.10	98.3	4.2	8.9	3.7	37.2	1.20e+05	2.48e+05	3.4	9.9	1.29e+04	4.72e+04
149	28.19	-0.04	97.8	4.4	9.2	1.3	19.5	8.26e+04	8.32e+04	1.5	3.4	1.27e+03	9.21e+03
150	28.24	-0.38	45.9	6.0	3.0	1.8	13.8	9.51e+03	2.60e+04	2.0	0.7	3.54e+01	5.92e+02

Table 1
(Continued)

SRBY	Within SRBY Defined Area, A_1									Within Half-Max Isophote of $N(\text{H}_2)$, A_2			
	l (deg)	b (deg)	v_o (km s $^{-1}$)	R_g (kpc)	Dist (kpc)	σ_v (km s $^{-1}$)	R (pc)	L_{CO} (K km s $^{-1}$ pc 2)	M_{LTE} (M_\odot)	σ_v (km s $^{-1}$)	R (pc)	L_{CO} (K km s $^{-1}$ pc 2)	M_{LTE} (M_\odot)
151	28.32	-0.06	78.0	4.8	5.0	3.5	24.3	9.22e+04	2.23e+05	3.3	4.7	4.07e+03	1.70e+04
152	28.61	0.05	101.3	4.3	8.8	4.1	26.5	1.48e+05	2.16e+05	4.4	4.4	4.24e+03	1.87e+04
153	28.79	0.19	81.9	4.9	10.1	3.2	16.6	5.08e+04	6.74e+04	3.1	8.1	8.35e+03	3.04e+04
154	28.80	-0.26	87.7	4.6	5.3	0.8	16.3	5.09e+04	3.15e+04	1.1	2.2	5.95e+02	4.21e+03
155	28.98	-0.27	93.9	4.5	5.7	2.5	31.6	7.30e+04	1.82e+05	3.5	3.4	1.94e+03	1.47e+04
156	28.99	-0.67	51.1	5.9	3.3	1.9	9.4	4.26e+03	9.35e+03	1.6	1.6	1.66e+02	1.73e+03
157	29.35	-0.46	78.7	5.0	4.7	2.5	23.8	7.22e+04	9.68e+04	2.8	1.3	4.46e+02	1.98e+03
158	29.01	0.05	96.9	4.4	8.9	2.9	41.1	1.90e+05	3.74e+05	3.0	3.5	1.64e+03	7.12e+03
159	29.32	-0.57	63.9	5.4	4.0	1.7	14.0	1.49e+04	2.82e+04	1.8	4.5	1.36e+03	7.51e+03
160	29.50	0.17	79.6	4.9	4.8	2.4	19.9	3.31e+04	5.87e+04	2.4	8.5	9.00e+03	2.87e+04
161	29.61	-0.61	75.6	5.0	10.2	2.9	40.8	1.45e+05	2.69e+05	2.0	6.1	2.54e+03	2.67e+04
162	29.89	-0.06	99.0	4.4	8.5	4.5	34.9	2.81e+05	8.28e+05	4.1	6.0	1.14e+04	1.17e+05
163	29.90	0.10	39.3	6.4	12.2	2.1	12.9	1.75e+04	3.45e+04	2.0	7.0	3.33e+03	1.56e+04
164	29.91	-0.77	83.7	4.8	5.1	1.1	13.2	6.72e+03	2.04e+04	1.2	0.9	3.96e+01	1.44e+03
165	30.41	0.46	45.1	6.2	2.8	1.2	5.0	1.39e+03	1.67e+03	1.4	1.4	1.45e+02	6.63e+02
167	30.56	0.32	92.2	4.5	8.7	1.9	26.1	9.42e+04	8.70e+04	1.9	2.5	3.05e+02	2.37e+03
168	30.57	-0.02	40.8	6.3	11.9	2.9	44.7	1.47e+05	2.69e+05	3.0	2.8	8.95e+02	1.07e+04
169	30.61	-0.45	94.0	4.6	8.8	2.4	14.4	4.99e+04	3.35e+04	2.5	8.6	1.18e+04	3.81e+04
170	30.59	-0.11	115.5	4.3	7.3	0.8	19.4	3.54e+04	3.17e+04	1.1	1.7	1.67e+02	1.90e+03
171	30.77	-0.01	94.2	4.6	5.7	6.8	41.8	3.17e+05	1.10e+06	5.7	5.2	1.11e+04	7.59e+04
172	30.83	-0.18	51.6	5.9	3.3	1.8	8.8	3.06e+03	6.90e+03	1.5	0.4	6.16e+00	3.12e+02
173	30.89	-0.60	102.0	4.4	7.9	0.7	8.4	6.67e+03	2.61e+03	0.9	2.2	3.23e+02	7.74e+02
174	30.96	0.09	39.5	6.5	12.1	3.3	36.2	1.30e+05	2.22e+05	2.1	3.3	1.07e+03	6.60e+03
175	30.97	0.40	79.7	5.1	4.7	2.6	12.5	2.13e+04	3.96e+04	2.3	1.1	1.04e+02	1.08e+03
177	31.28	-0.00	79.7	5.0	4.9	3.2	14.7	2.66e+04	4.84e+04	3.2	5.4	3.96e+03	1.48e+04
178	31.32	-0.03	41.0	6.6	12.1	3.7	58.6	2.43e+05	5.06e+05	3.5	7.7	5.88e+03	4.31e+04
179	31.39	-0.26	87.9	4.8	9.1	1.6	13.6	1.84e+04	1.63e+04	1.7	2.8	6.69e+02	4.06e+03
180	31.44	0.08	106.0	4.4	7.3	2.6	21.9	6.62e+04	8.94e+04	3.0	3.2	1.77e+03	1.31e+04
181	31.98	-0.28	97.5	4.6	8.1	2.5	19.0	3.62e+04	3.08e+04	2.6	7.4	5.03e+03	1.28e+04
182	32.02	0.06	96.8	4.6	8.0	2.1	37.7	8.93e+04	1.57e+05	2.5	3.3	1.91e+03	1.54e+04
183	32.46	0.22	50.6	6.1	11.2	1.4	15.0	2.20e+04	4.02e+04	1.5	2.0	2.40e+02	3.39e+03
184	32.70	-0.18	92.5	4.8	8.6	1.7	44.4	1.58e+05	1.38e+05	1.5	3.0	7.47e+02	5.32e+03
185	33.38	-0.53	91.2	4.8	8.2	1.6	23.0	2.24e+04	2.81e+04	1.5	6.3	2.41e+03	8.63e+03
186	33.36	-0.00	72.9	5.3	9.6	2.4	34.0	8.36e+04	1.06e+05	2.2	5.5	3.46e+03	9.11e+03
187	33.44	-0.08	86.5	4.9	8.7	2.2	35.7	8.99e+04	1.14e+05	2.2	11.4	9.66e+03	2.40e+04
188	33.79	-0.18	52.4	6.3	11.2	3.4	32.9	6.16e+04	1.16e+05	3.1	5.6	2.71e+03	1.16e+04
189	33.66	0.22	41.7	6.5	11.6	1.5	21.3	2.41e+04	3.11e+04	1.2	3.3	4.22e+02	3.04e+03
190	33.85	0.00	89.2	4.9	8.4	1.2	19.9	3.48e+04	2.48e+04	1.2	12.1	8.33e+03	1.44e+04
191	33.83	0.07	105.6	4.7	7.1	2.2	30.1	6.69e+04	7.76e+04	2.0	2.1	4.74e+02	2.83e+03
192	34.16	-0.10	88.1	4.9	8.3	2.1	21.5	4.01e+04	3.56e+04	1.9	6.0	2.26e+03	9.18e+03

Table 1
(Continued)

SRBY	Within SRBY Defined Area, A_1									Within Half-Max Isophote of $N(\text{H}_2)$, A_2			
	l (deg)	b (deg)	v_o (km s $^{-1}$)	R_g (kpc)	Dist (kpc)	σ_v (km s $^{-1}$)	R (pc)	L_{CO} (K km s $^{-1}$ pc 2)	M_{LTE} (M_\odot)	σ_v (km s $^{-1}$)	R (pc)	L_{CO} (K km s $^{-1}$ pc 2)	M_{LTE} (M_\odot)
193	34.20	0.12	57.5	6.1	3.2	2.8	18.1	3.00e+04	1.07e+05	2.8	1.4	1.68e+02	1.70e+04
195	34.36	-0.19	52.2	6.1	3.2	2.3	7.6	3.37e+03	7.86e+03	2.3	2.7	5.94e+02	2.58e+03
196	34.76	-0.13	78.9	5.3	4.8	3.3	16.1	1.59e+04	3.37e+04	3.6	3.7	1.32e+03	5.67e+03
198	34.99	0.33	51.8	6.2	3.1	1.0	15.7	2.31e+04	3.60e+04	1.3	0.7	4.54e+01	8.03e+02
202	35.66	0.15	81.7	5.2	8.5	2.7	36.0	9.81e+04	1.43e+05	2.2	2.1	3.41e+02	4.21e+03
203	35.79	-0.16	28.8	7.2	1.7	1.2	12.8	3.80e+03	7.76e+03	0.9	0.6	6.14e+00	5.66e+02
204	35.97	-0.48	58.7	6.0	3.5	1.7	6.4	3.69e+03	4.50e+03	1.6	2.5	4.44e+02	2.00e+03
205	36.13	0.66	77.5	5.4	4.9	3.6	31.7	5.58e+04	7.36e+04	2.2	1.5	1.91e+02	1.30e+03
206	36.42	-0.10	54.8	6.3	3.1	2.0	17.2	2.74e+04	5.13e+04	1.8	3.6	9.23e+02	5.00e+03
207	36.49	-0.11	78.6	5.4	4.9	3.1	25.3	3.51e+04	5.95e+04	2.3	2.0	2.90e+02	2.10e+03
208	36.90	-0.07	79.9	5.3	5.2	2.2	13.9	1.81e+04	3.66e+04	2.1	6.4	4.24e+03	1.58e+04
209	37.38	0.17	87.2	5.2	6.8	3.1	31.8	7.05e+04	1.24e+05	2.7	1.4	1.02e+02	5.27e+03
210	37.49	0.08	41.9	6.7	2.4	1.6	6.4	1.92e+03	2.95e+03	0.9	0.5	3.97e+00	2.92e+02
211	37.76	-0.21	62.8	6.0	9.8	3.4	20.8	5.01e+04	7.71e+04	3.1	3.2	1.14e+03	8.41e+03
212	38.23	-0.15	62.9	5.9	9.3	2.7	10.8	2.13e+04	3.16e+04	2.9	5.1	2.78e+03	1.38e+04
213	38.93	-0.45	41.7	6.8	2.5	1.5	10.8	9.17e+03	2.28e+04	1.4	1.0	1.52e+02	1.29e+03
214	39.83	-0.28	60.3	6.2	9.6	3.8	90.8	7.72e+05	1.19e+06	3.4	15.1	2.81e+04	1.08e+05
215	40.32	-0.42	73.5	5.7	5.0	0.9	12.5	8.05e+03	8.35e+03	1.0	1.2	5.75e+01	5.59e+02
216	41.05	-0.17	39.8	7.0	2.2	1.8	11.4	8.01e+03	1.29e+04	1.9	3.5	7.76e+02	3.28e+03
217	41.18	-0.22	61.1	6.2	9.0	1.8	42.6	1.99e+05	2.52e+05	1.5	1.5	1.98e+02	3.73e+03
218	41.89	-0.40	60.3	6.2	8.9	1.4	25.3	5.69e+04	6.72e+04	1.6	5.8	2.60e+03	9.71e+03
219	42.34	-0.08	57.5	6.3	8.9	3.0	20.6	5.06e+04	6.33e+04	2.7	3.5	1.11e+03	4.59e+03
220	42.15	-0.60	67.2	6.0	4.5	2.2	15.9	2.84e+04	5.52e+04	1.7	0.3	4.58e+00	3.59e+02
221	42.72	-0.35	62.6	6.3	3.8	3.8	16.9	1.97e+04	5.74e+04	3.5	1.5	1.46e+02	1.11e+03
223	43.17	-0.52	57.9	6.4	3.6	1.2	7.1	2.56e+03	6.79e+03	1.5	0.5	2.22e+01	1.34e+03
224	44.38	-0.22	61.2	6.2	7.7	4.0	46.1	1.91e+05	4.59e+05	2.3	0.8	4.67e+01	2.68e+03
225	45.44	0.07	59.9	6.4	8.1	4.4	47.0	1.66e+05	4.43e+05	3.0	3.6	2.03e+03	2.03e+04
226	46.32	-0.20	55.0	6.4	7.7	3.4	13.6	1.42e+04	5.82e+04	2.5	1.5	1.41e+02	3.43e+03
227	47.05	0.26	57.6	6.6	7.9	2.1	19.8	2.15e+04	6.81e+04	1.7	2.2	2.63e+02	1.29e+04
229	47.55	-0.54	59.1	6.4	7.2	1.7	17.7	1.97e+04	1.95e+04	1.6	3.7	5.69e+02	3.32e+03
232	48.83	0.14	52.6	6.7	7.7	1.9	32.0	3.42e+04	1.28e+05	1.5	2.0	2.25e+02	2.98e+03
234	49.74	-0.52	68.1	6.5	5.5	1.1	11.9	9.88e+03	1.89e+04	0.9	2.7	4.92e+02	2.61e+03
236	50.83	0.25	42.3	7.0	2.9	2.0	7.3	2.62e+03	7.69e+03	1.6	0.7	1.79e+01	7.96e+02
237	51.33	-0.04	54.7	6.7	6.2	2.5	31.3	6.05e+04	9.99e+04	1.9	0.8	4.53e+01	4.28e+03
238	52.30	-0.06	51.1	6.8	6.1	1.6	12.3	1.38e+04	1.90e+04	1.6	5.2	1.63e+03	6.23e+03
240	53.17	-0.25	62.7	6.8	5.1	2.3	9.0	8.71e+03	1.28e+04	1.9	1.3	1.32e+02	1.37e+03
241	53.43	0.07	23.3	7.7	1.5	1.1	15.9	5.19e+03	2.26e+04	0.9	0.2	6.26e+00	2.72e+02
242	54.12	-0.07	39.1	7.2	7.0	2.5	12.8	1.24e+04	5.03e+04	2.3	3.5	1.84e+03	1.95e+04
243	54.66	0.81	32.8	7.5	7.7	2.9	28.2	4.33e+04	1.12e+05	2.8	7.3	5.11e+03	2.17e+04

(This table is also available in a machine-readable form in the online journal.)

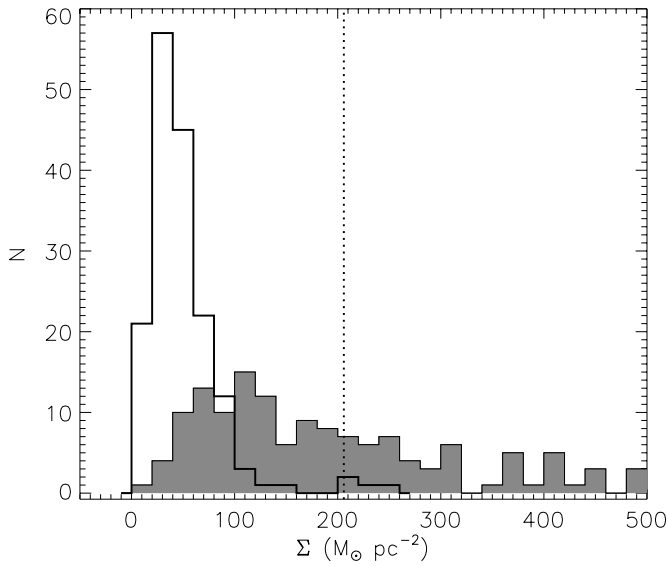


Figure 4. Histogram of cloud mass surface densities derived from ^{13}CO data and assuming LTE and a constant H_2 to ^{12}CO abundance ratio within areas, A_1 (heavy line) and A_2 (shaded). The vertical dotted line denotes the median surface density from SRBY.

2.2. GMC Surface Densities

The surface density of a molecular cloud is a key property to its evolution and dynamical state (McKee & Ostriker 2007). The GMC surface density is simply the mass of the cloud divided by the projected area. Since we are tabulating masses within the same area as SRBY, the discrepancies in masses, discussed in the previous section, are mirrored in the resultant mass surface densities. The distribution of LTE-derived surface densities determined within the SRBY defined areas is shown in Figure 4. Also shown is the distribution of mass surface density values within the half-power isophote of column density, A_2 . The vertical dotted line shows the median surface density determined by SRBY. For area A_2 that tracks the highest column density zones within each GMC, the LTE-derived surface densities are comparable to the SRBY values that consider the entire GMC. The median surface density implied by the LTE-derived masses within A_1 is $42 M_\odot \text{pc}^{-2}$ with a standard deviation of $37 M_\odot \text{pc}^{-2}$. There are several reasons to expect a limited variation of GMC surface densities derived from a given gas tracer. First, for a given UV radiation field, there is a minimum column density necessary to self-shield H_2 and ^{12}CO in order to build and maintain significant molecular abundances. Second, high-density regions (cores) within a GMC subtend a small fraction of the projected area of a cloud and do not significantly contribute to the overall mass. Moreover, owing to high optical depths and chemical depletion, such regions are not readily detected by ^{12}CO or ^{13}CO . Therefore, one expects to find a limited range of molecular surface densities corresponding to those required for molecular self-shielding within a given UV radiation field (Elmegreen 1989; McKee 1989).

2.3. Errors and Uncertainties in H_2 Mass Determinations

The large differences in mass and surface density of GMCs derived by SRBY and this study suggest that one or both methods are subject to errors. The differences are not due to instrumental errors of the CO measurements. Masses are integrated quantities so the statistical errors are typically small

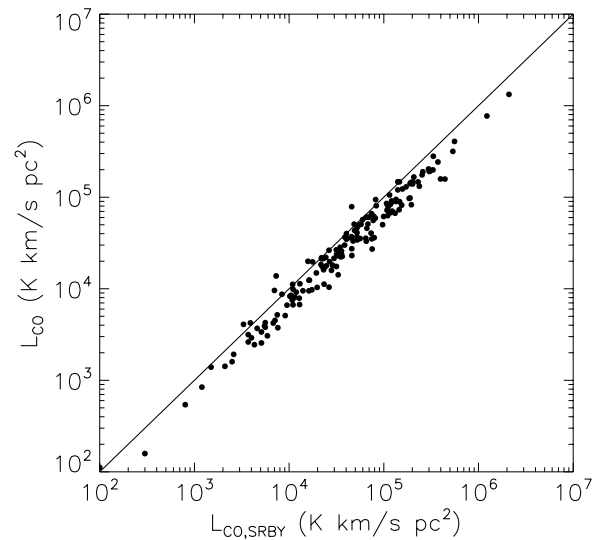


Figure 5. L_{CO} from the direct integration of the signal over the enclosed area vs. the CO luminosity from the SRBY catalog. The solid line shows $L_{\text{CO,SRBY}} = L_{\text{CO}}$. The smaller direct integration values of L_{CO} suggest that the extrapolated values overestimate the true value.

(1%–10%). However, both methods are affected by systematic errors, which we now summarize.

The SRBY estimates of cloud virial masses rely on the accurate extrapolation of cloud properties, σ_v , R , from the values defined at the 4 K or higher threshold of antenna temperature to the 1 K isophote that presumably circumscribes the bulk of the GMC. For such an extrapolation to succeed, the measured variation of the cloud properties (CO luminosity, size, velocity dispersion) with antenna temperature above the 4 K threshold must accurately reflect the structure of the cloud at all antenna temperature values. However, the profile of these values above the 4 K threshold is limited by the angular undersampling of the UMSB survey and the opacity of the CO $J = 1-0$ line. Figure 1 demonstrates that the undersampled UMSB data misses much of the underlying structure of the cloud, especially within the brightest subregions, where the cloud is presumably defined at the 4 K limit by SRBY. The primary effect of undersampling is aliasing of small-scale structure to larger scales. This aliasing affects the inferred variation of cloud properties with antenna temperature. For example, the $3'$ sampling with $45''$ resolution is unlikely to accurately measure the position and amplitude of localized emission peaks or troughs within the cloud yet must assign any detected signal to a solid angle defined by the sampling interval. By not accounting for small-scale structure, the derived variations of velocity dispersion, size, and luminosity with antenna temperature are less reliable. In addition, $^{12}\text{CO } J = 1-0$ emission is strongly saturated owing to high optical depth. Not only does high opacity obscure underlying cloud structure, but line saturation also flattens the surface brightness profile. The corresponding extrapolation of shallow profiles induced by high optical depth of the ^{12}CO line leads to overestimates of cloud sizes and CO luminosities at the 1 K isophote.

A comparison of the extrapolated values of the CO luminosity, $L_{\text{CO,SRBY}}$, as listed in the catalog, and a direct measure, L_{CO} , determined from the integration of the UMSB CO intensities within the cloud boundaries and velocity intervals, is shown in Figure 5. The extrapolated values are typically 35% larger than the direct measures of L_{CO} . Such higher values are unexpected

given that the direct measure should be contaminated by signal from unrelated clouds along the line of sight over the same velocity range. This suggests that the extrapolated values of the CO luminosity are systematically overestimating the true CO luminosity. Similarly, the extrapolated cloud sizes and velocity dispersions that are used to derive the virial mass may also be inappropriate.

Masses and H_2 column densities assuming LTE are also subject to several sources of systematic error. First, the assumption of equal ^{12}CO and ^{13}CO excitation temperatures is not valid for the full range of volume densities within molecular clouds. Such excitation differences arise from the relative optical depths of the two lines such that these may not sample the same volumes and conditions within the cloud. For densities less than the CO critical density ($n(\text{H}_2) < 750 \text{ cm}^{-3}$), the $^{12}\text{CO } J = 1-0$ line can be thermalized by radiative trapping while the $^{13}\text{CO } J = 1-0$ line remains subthermally excited. Overestimating the ^{13}CO excitation temperature leads to an underestimation of the $^{13}\text{CO } J = 1-0$ opacity. Second, the excitation of the rotational energy levels of ^{13}CO is not fully thermalized for most of the cloud volume. For densities less than $5 \times 10^5 \text{ cm}^{-3}$, the approximation of the partition function, $\sum_{J=0}^{\infty} (2J+1) \exp(-J(J+1)hB/kT_x) = kT/hB$, to account for material within the upper excitation states, overcorrects for the upper population energy levels.

To examine these effects more quantitatively, we generate model ^{12}CO and ^{13}CO line intensities for several sets of cloud conditions using a large velocity gradient (LVG) approximation to account for non-thermal excitation. The input model parameters are kinetic temperature, H_2 column density, N_{model} , H_2 volume density, $n(\text{H}_2)$, ^{12}CO and ^{13}CO abundance, and velocity dispersion. The filling factor of both ^{12}CO and ^{13}CO emission is assumed to be unity. For each model, the output ^{12}CO and ^{13}CO line intensities are used to derive an LTE H_2 column density, N_{LTE} , that can be compared with the input value. Figure 6 shows the fraction of column density recovered by the LTE method as a function of volume density for models with kinetic temperatures of 8 and 15 K, H_2 to ^{12}CO abundance of 1.1×10^4 , a ^{12}CO to ^{13}CO abundance of 50, velocity dispersion of 2 km s^{-1} , for two values of N_{model} . In the low-density regime ($n(\text{H}_2) < 400 \text{ cm}^{-3}$), the models illustrate that the LTE method underestimates the input column density by factors of ~ 2 owing to an inappropriately high excitation temperature estimated from the ^{12}CO line intensity that leads to a reduced value of the ^{13}CO opacity. This effect is more pronounced for the models with 8 K kinetic temperature. With increasing density, the $^{13}\text{CO } J = 1-0$ line becomes progressively thermalized such that the ^{13}CO opacity is more accurately determined but the upper rotational energy levels remain subthermally excited. In this regime, LTE overestimates the column density by 10%–40%. A similar result is obtained by Pineda et al. (2008) and Goodman et al. (2008), who used a simple curve of growth analysis to demonstrate that the ^{13}CO integrated emission increases more rapidly with extinction in the low column density regime. If these intensities are multiplied by a conversion factor derived from a linear fit over the full range of extinction, then the resultant column densities may overestimate the true values. In the high-density limit ($n(\text{H}_2) > 2 \times 10^5 \text{ cm}^{-3}$), the assumption of LTE is valid such that $N_{\text{LTE}}/N_{\text{model}} = 1$. The models illustrate that column densities derived from ^{12}CO and $^{13}\text{CO } J = 1-0$ measurements assuming LTE can both underestimate or overestimate the true column densities depending on the physical conditions of the cloud.

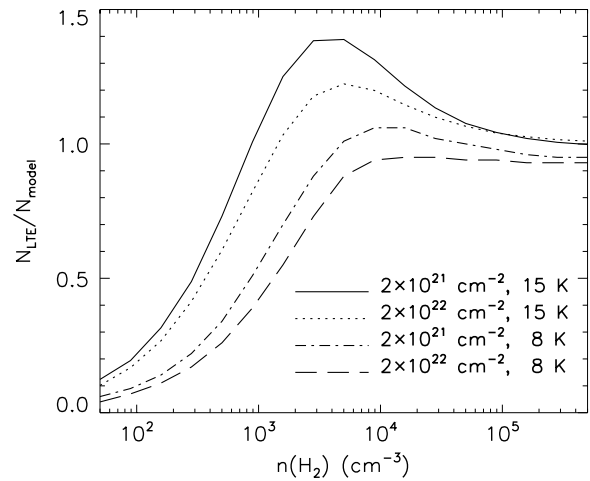


Figure 6. Variation of the fraction of column density recovered by the LTE method, $N_{\text{LTE}}/N_{\text{model}}$, with volume density as derived from LVG models with model column densities of $2 \times 10^{21} \text{ cm}^{-2}$ and $2 \times 10^{22} \text{ cm}^{-2}$, kinetic temperatures of 8 K and 15 K, velocity dispersion of 2 km s^{-1} , and constant ^{12}CO and ^{13}CO abundances. Over the range of densities expected for the bulk of molecular clouds ($500 \text{ cm}^{-3} < n(\text{H}_2) < 5000 \text{ cm}^{-3}$), the LTE method can both underestimate and overestimate the gas column density owing to varying degrees of excitation.

The assumption of constant abundance of CO relative to molecular hydrogen within a cloud is another source of error in our application of the LTE method. CO abundances can strongly vary between the strongly self-shielded interiors and the UV-exposed envelope owing to selective photodissociation and fractionation (van Dishoeck & Black 1988; Liszt 2007). The effect of reduced CO to H_2 abundances in the cloud envelope is to mask regions that contain high column densities of H_2 but radiate no detectable $^{13}\text{CO } J = 1-0$ emission. For example, the solid curve in Figure 6 corresponding to $N_{\text{model}} = 2 \times 10^{21} \text{ cm}^{-2}$ is degenerate with an H_2 column density of $2 \times 10^{22} \text{ cm}^{-2}$ and an H_2 to ^{12}CO abundance of 1.1×10^5 . For densities less than 500 cm^{-3} , the predicted ^{13}CO emission is less than 0.55 K and would not be detected by the GRS at a 3σ confidence level. By not considering these abundance variations our LTE-derived GMC masses may underestimate the true values. There is insufficient information with these data to uniquely quantify this error. In a recent study of the Taurus molecular cloud, Goldsmith et al. (2008) show that this subthermally excited, UV-exposed envelope with no detectable ^{13}CO emission can contribute as much as 50% of the cloud's mass when accounting for such molecular abundance variations. Based on this example and the fraction of area with detectable ^{13}CO emission within the SRBY boundaries, the true values of GMC mass and mass surface density could be larger by factors of 2–3 than the LTE-derived values.

A commonly used validation of the SRBY estimates of cloud masses and surface densities is the consistency with the CO intensity to H_2 conversion factor, X_{CO} , derived from γ -ray measurements (Bloemen et al. 1986). In fact, their implied value of $X_{\text{CO}} = M_{v,\text{SRBY}}/L_{\text{CO,SRBY}}$ varies by a factor of 2 over the luminosity range of the sample owing to the $4/5$ power law relationships dependence of $M_{v,\text{SRBY}}$ on $L_{\text{CO,SRBY}}$. For the median SRBY luminosity of $4.3 \times 10^4 \text{ K km s}^{-1} \text{ pc}^2$, the SRBY conversion factor is $5.7 M_{\odot}/(\text{K km s}^{-1} \text{ pc}^2)$ or equivalently, $2.7 \times 10^{20} \text{ H}_2 \text{ molecules cm}^{-2}/(\text{K km s}^{-1})$, accounting for the contributions of helium. More recent estimates of X_{CO} from γ -ray measurements indicate a lower value, $X_{\text{CO}} = 4M_{\odot}/$

(K km s⁻¹ pc²), which corresponds to 1.9×10^{20} H₂ molecules cm⁻² (K km s⁻¹) (Strong & Mattox 1996). The implied SRBY H₂ column density is 9.7×10^{21} cm⁻² corresponding to a ¹²CO surface brightness within the cloud boundaries of 51 K km s⁻¹ assuming this most recent CO to H₂ conversion factor. We have calculated the ¹²CO surface brightness for each cloud, $\iint dv dA T(l, b, v) / \int dA$ using the UMSB data. The median of the distribution of GMC surface brightness values is 30 K km s⁻¹. This difference is evident for the three clouds shown in Figure 1, where the color lookup table for the ¹²CO images is set so all pixels above 50 K km s⁻¹ should be saturated. Only a small fraction of pixels exceed this value. Cloud blending should only increase the mean surface brightness of each cloud as more of the SRBY defined area is filled by emission from unrelated clouds. Either the extrapolated SRBY column densities are too large or the ¹²CO–H₂ conversion factor is too small to be consistent with the observed surface brightness distributions.

How do the newly derived LTE masses compare with the X factor? M_{LTE} is linearly correlated with L_{CO} in contrast to the 4/5 power law relationships found by SRBY. The median value of $M_{\text{LTE}}/L_{\text{CO}}$ is $1.6 M_{\odot}/(\text{K km s}^{-1} \text{ pc}^2)$. However, M_{LTE} is likely a lower limit due to the neglect of abundance variations within the outer envelope. If $M_{\text{GMC}} \sim 2M_{\text{LTE}}$, as suggested by local cloud studies, then these rescaled LTE-derived column density estimates are compatible with the value of X_{CO} determined from γ -rays.

3. DISCUSSION

The GMC masses derived in this study are systematically lower than those estimated by SRBY. These lower values have significant implications to the global molecular content of the Galaxy. Solomon & Rivolo (1989) provide a detailed summary of the biases and completeness inherent in their cloud definition. They demonstrate that the SRBY catalog is complete to a limiting mass of $2.5 \times 10^5 M_{\odot}$ (corrected for current Galactic distances). Accounting for Malmquist bias effects, they estimate that the SRBY clouds account for 40% of the total CO luminosity and 40% of the flux of the UMSB Survey. The remaining 60% of the CO luminosity and flux is presumed to originate from cold and/or small clouds that fall below their GMC identification threshold. The mass distribution, $dN(M)/dM$, of GMCs follows a power law relationships, $dN/dM \sim M^{-\alpha_M}$ with α_M ranging from 1.5 (SRBY) to 1.8 (Heyer et al. 2001). The measured slopes of the GMC mass function imply that most of the molecular mass in the Galaxy resides within the largest clouds that are included in the SRBY sample. Yet, our new calculations of cloud masses imply that the true masses are smaller than the SRBY values by factors of 2–5 depending on the correction for subthermally excited gas and varying abundances within a cloud. Such a rescaling of GMC masses implies a reduced molecular mass content of the Galaxy by these same factors.

Could there be a significant molecular gas mass component residing within smaller, cooler clouds that were not included in the SRBY catalog? Owing to higher angular sampling than the UMSB survey, the GRS is more sensitive to smaller clouds. A comparison of the GRS field with SRBY clouds does indeed show both discrete and diffuse features that are not included within the SRBY catalog. Yet, we find that 32% of the ¹³CO emission over the GRS field originates within SRBY cloud boundaries, which is comparable to the value (40%) estimated

by Solomon & Rivolo (1989) for ¹²CO. The emission from volumes external to the SRBY boundaries may provide a significant and unaccounted reservoir of molecular material within the Galaxy.

The molecular gas fraction depends on both the surface density of the cloud and the ambient radiation field (Elmegreen 1989; van Dishoeck & Black 1988). Significant abundances of H₂ and CO require sufficient column densities to self-shield. It is possible that the fraction of LTE-derived mass to the SRBY-derived virial masses, $M_{\text{LTE}}/M_{v, \text{SRBY}}$, and the higher SRBY surface densities reflect a more intense ambient radiation field in the inner Galaxy owing to higher star-formation activity relative to the solar neighborhood. In this case, one would expect to find a dependence of this fraction on galactocentric radius. However, we find no evidence for any variation of this fraction over the range of radii (4.1–8.1 kpc) of the cloud sample.

3.1. Re-Examining Larson's Scaling Relationships

The scaling relationships identified by Larson (1981) have provided a fundamental, observational constraint to descriptions of cloud dynamics and star formation. The study by SRBY seemingly confirmed these scaling relationships for a larger sample of molecular clouds distributed throughout the Galaxy. Given the results in the previous section, which demonstrate that the SRBY GMC masses and surface densities are likely overestimates to the true values, it is useful to re-examine the Larson (1981) scaling relationships with the new GRS data within the SRBY defined cloud boundaries.

As has been demonstrated by many previous studies, the Larson scaling relationships are algebraically linked. Here, we re-summarize this coupling to derive the coefficients that are critical to the interpretation of cloud dynamics. Gravitational equilibrium (Larson's second relationship) implies that the observed mass of the cloud, M_{obs} , is equal to the virial mass,

$$M_{\text{obs}} = 5\sigma_v^2 R / G. \quad (8)$$

The cloud size, R , is defined as the radius of a circle with the equivalent area of the cloud. The molecular gas surface density, Σ , of a cloud is simply the H₂ mass divided by the projected area,

$$\Sigma = \frac{M_{\text{obs}}}{\pi R^2}. \quad (9)$$

Eliminating M_{obs} and solving for σ_v ,

$$\sigma_v = (\pi G / 5)^{1/2} \Sigma^{1/2} R^{1/2}. \quad (10)$$

If Σ is approximately constant for all clouds (Larson's third relationship), then one recovers the size–line width scaling (Larson's first relationship), $\sigma_v = v_{\circ, G} R^{1/2}$, with the normalization coefficient

$$v_{\circ, G} = (\pi G \Sigma / 5)^{1/2}, \quad (11)$$

$$v_{\circ, G} = 0.52 \left(\frac{\Sigma}{10^2 M_{\odot} \text{ pc}^{-2}} \right)^{1/2} \text{ km s}^{-1} \text{ pc}^{-1/2}. \quad (12)$$

The coefficient, $v_{\circ, G}$, parameterizes the scaling of velocities within a cloud such that non-thermal pressure balances the self-gravity of the cloud with surface density, Σ , and radius, R .

More generally, the velocity field of an interstellar cloud is described by the structure function that measures the variation of velocity differences of order p , with spatial scale, τ ,

$$S_p(\tau) = \langle |v(\mathbf{x}) - v(\mathbf{x} + \tau)|^p \rangle, \quad (13)$$

where the angle brackets denote a spatial average over the observed field. Within the inertial range, the structure function is expected to vary as a power law relationships with τ . For $p = 1$,

$$S_1(\tau) = \delta v = v_o \tau^\gamma, \quad (14)$$

where γ is the scaling exponent and v_o is the scaling coefficient. These parameters correspond to Type 4 size–line width relationships described by Goodman et al. (1998). The velocity dispersion¹ of an individual cloud is simply the structure function evaluated at its cloud size, L , such that $\sigma_v = S_1(L) = v_o L^\gamma$. Cloud-to-cloud size–velocity dispersion relationships, defined as Type 2 by Goodman et al. (1998), are constructed from the endpoints of each cloud’s velocity structure function. The existence of a cloud-to-cloud size–velocity dispersion relationship identified by SRBY necessarily implies narrow distributions of the scaling exponent and coefficient, respectively, for all clouds (Heyer & Brunt 2004). Large variations of v_o and γ between clouds would induce a large scatter of points that is inconsistent with the observations. From Monte Carlo modeling of the scatter of the SRBY size–velocity dispersion relationship, Heyer & Brunt (2004) constrained the variation of γ and v_o between clouds to be less than 20% about the mean values that is indicative of a universal structure function. This universality is also reflected in the structure functions of individual clouds as derived by Brunt (2003) and Heyer & Brunt (2004) using principal component analysis.

The Larson scaling relationships are concisely represented within the plane defined by the gas surface density, Σ , and the quantity, $\sigma_v/R^{1/2}$, for a set of GMC properties (see Equation (10)). This representation assumes a scaling exponent of 1/2 for the structure function of each cloud so that the ordinate, $\sigma_v/R^{1/2}$, is equivalent to the scaling coefficient, v_o . Absolute adherence to universality and all three of Larson’s scaling relationships for a set of clouds would be ideally represented by a single point centered at $\sigma_v/R^{1/2} = (\pi G \Sigma/5)^{1/2}$ for a constant value of Σ . Given uncertainties in distance and deriving surface densities, one more realistically expects a cluster of points at this location. In Figure 7, we show the corresponding points derived from the GRS data within the SRBY boundaries (area A_1) and the area within the half-power isophote of N_{H_2} (area A_2). The vertical error bars displayed in the legend reflect a 20% uncertainty in the distance to each cloud. As a reference point, the large triangle denotes the location of the SRBY median values ($\sigma_v/R^{1/2} = 0.72 \text{ km s}^{-1}$; $\Sigma(\text{H}_2) = 206 M_\odot \text{ pc}^{-2}$). The solid line shows the loci of points assuming gravitationally bound clouds, $\sigma_v/R^{1/2} = (\pi G/5)^{1/2} \Sigma^{1/2}$, that is nearly identical to the coefficients used by SRBY. For both considered cloud areas, the ^{13}CO data points are displaced from this loci of virial equilibrium. The median virial parameter, $\alpha_G = M_{v,13}/M_{\text{LTE}}$, is 1.9, where $M_{v,13}$ is the virial mass derived from ^{13}CO data within A_1 . However, the LTE-derived mass could underestimate the true cloud mass by factors of 2–3 as suggested in Section 2, so the derived properties are consistent with a virial parameter of unity for this sample of clouds.

Figure 7 reveals a systematic variation of $v_o = \sigma_v/R^{1/2}$ with Σ . This trend is separately evident for each area, A_1 (open circles) and A_2 (filled circles) with Pearson correlation coefficients 0.48 and 0.65, respectively. For these sample sizes, it is improbable that these data sets are drawn from a random population. The

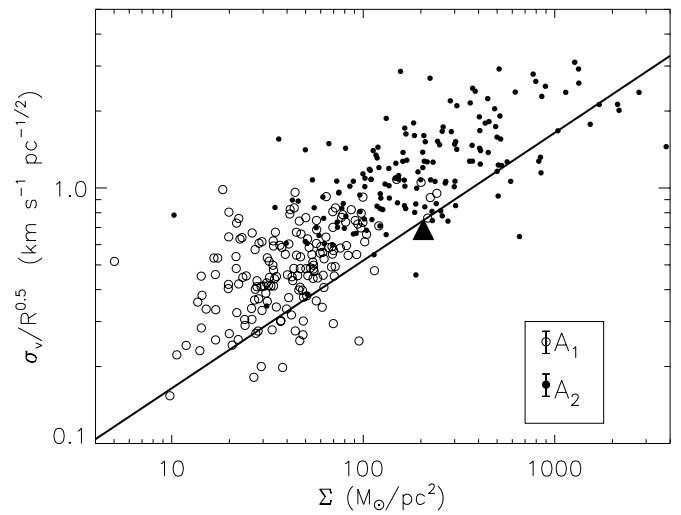


Figure 7. Variation of the scaling coefficient, $v_o = \sigma_v/R^{1/2}$, with mass surface density derived within the SRBY cloud boundaries (open circles) and the 1/2 maximum isophote of H_2 column density (filled circles). The filled triangle denotes the value derived by SRBY. The solid line shows the loci of points corresponding to gravitationally bound clouds. There is a dependence of the coefficient with mass surface density in contrast to Larson’s velocity scaling relationship. The error bars in the legend reflect a 20% uncertainty of the distance to each cloud.

dependence of $\sigma_v/R^{1/2}$ on Σ signals a departure from the universality of the velocity structure function of clouds. It implies a necessary modification to Larson’s scaling relationships but one that is compatible with the rather basic premise of gravitational equilibrium as described in Equation (10). The measured variation of $v_o = \sigma_v/R^{1/2}$ is larger than the values derived by Heyer & Brunt (2004) owing to the larger intrinsic scatter in the size–velocity dispersion relationship determined from the GRS data.

The dependence of $\sigma_v/R^{1/2}$ on Σ may not have been recognized in previous studies owing to a limited range of surface densities in the observed samples, or the use of a less reliable tracer of molecular gas column density, or simply not considered given the long-standing acceptance of Larson’s scaling relationships. The fidelity of the GRS data provides an excellent relative, if not absolute, measure of gas surface density that allows this relationship to be recognized. We note that this relationship is algebraically imposed when deriving surface densities from the virial mass, $\Sigma = M_{\text{vir}}/\pi R^2 \propto \sigma_v^2/R$, as calculated by SRBY. However, as shown in Figure 8, the relationship is even evident in the SRBY defined properties when using the mean ^{12}CO surface brightness and CO to H_2 conversion factor as a measure of gas surface density, $\Sigma = X_{\text{CO}} L_{\text{CO,SRBY}}/\Omega_1 D^2$, where Ω_1 is the solid angle of the cloud corresponding to A_1 and D is the distance. Moreover, the scaling between $\sigma_v/R^{1/2}$ and Σ is also present in the sample of extragalactic GMCs tabulated by Bolatto et al. (2008; filled squares in Figure 8). The presence of this scaling within these independent data sets offers a powerful verification that the velocity dispersion of a cloud depends on both the spatial scale of the emitting area and the mass surface density.

3.2. GMC Dynamics

Descriptions of cloud dynamics must consider the nature and origin of the observed supersonic motions in GMCs. While much of the theoretical effort has focused on the scaling exponent of the power spectrum or structure function of the

⁴ Cloud-to-cloud size–velocity dispersion relationships use the full velocity dispersion of the cloud but scaled to the cloud radius, $R \sim L/2$. Therefore, the respective definitions for the coefficient may differ by a factor of $\sim 2^\gamma$.

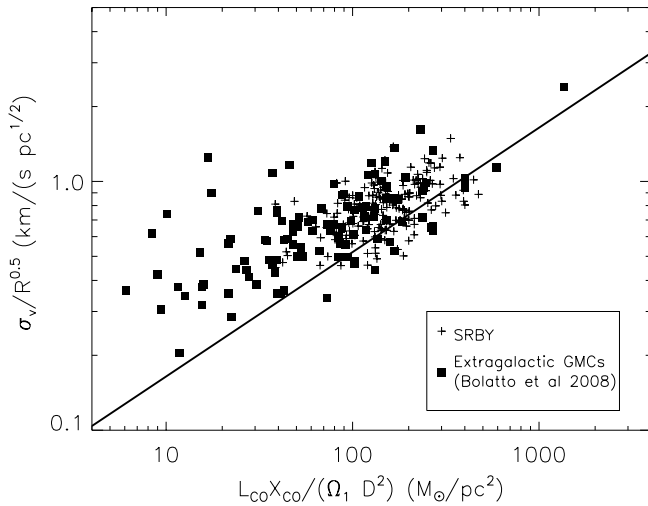


Figure 8. Variation of the scaling coefficient, $v_0 = \sigma_v / R^{1/2}$, with mass surface density for GMCs from the SRBY catalog (+ symbols) and extragalactic GMCs from Bolatto et al. (2008; filled squares).

velocity field, the normalization, v_0 , provides an important measure of the amplitude of these motions as it is evaluated at a fixed scale of 1 pc. Figure 7 illustrates an additional constraint to these descriptions—that for a given cloud, the amplitude of the motions depends on the mass surface density. It is not evident from the present measurements whether this variation of v_0 with Σ is due to varying evolutionary states of the sample clouds or one that reflects different cloud conditions owing to the environmental diversity of the ISM.

For sub-Alfvénic clouds whose neutral gas component is dynamically coupled to the interstellar magnetic field through ion–neutral collisions, the observed motions could arise from the propagation of large amplitude, long wavelength Alfvén waves through the cloud (Arons & Max 1975). In fact, a simple model of magnetically supported clouds in which the cloud surface density equals the magnetic critical surface density, $\Sigma_c = B / (63G)^{1/2}$, predicts the trend observed in Figure 7 (Mouschovias 1987; Myers & Goodman 1988a; Mouschovias & Psaltis 1995; Mouschovias et al. 2006). The observed variation of the coefficient with surface density simply reflects plausible differences of the magnetic field strength between clouds owing to Galactic environments and the support of the cloud by the magnetic field such that $\Sigma \approx \Sigma_c$. The vertical scatter of values for a given surface density would arise from varying flux-to-mass ratios owing to ambipolar diffusion.

A definitive test of the role of the interstellar magnetic field in the support of the cloud and the origin of observed internal motions requires measures of the magnetic field strength. Such measurements are not available for this set of GMCs. Myers & Goodman (1988b) demonstrate that the magnetic field strength derived from thermal OH Zeeman measurements is comparable to the predicted field strength assuming equipartition between the magnetic, kinetic, and gravitational energies, $B_{eq} \approx (45/G)^{1/2} \sigma_v^2 / R$ for a set of nearby clouds.

4. SUMMARY

Our re-examination of the properties of GMCs in the Milky Way have identified two new results that challenge the long-standing assumptions of cloud dynamics.

1. The mass surface density of GMCs is lower than previously estimated by SRBY. Assuming a constant abundance of

molecular hydrogen to CO within a cloud, the median mass surface is $42 M_\odot \text{ pc}^{-2}$. Abundance variations within the outer envelope of clouds could increase the mass surface density to $80\text{--}120 M_\odot \text{ pc}^{-2}$. No dependence of mass surface density is found with galactocentric radius.

2. The normalization of the velocity structure function, derived from the velocity dispersion and the size of each cloud, $v_0 = \sigma_v / R^{1/2}$, varies with the molecular gas surface density, as $\Sigma^{1/2}$. The dependence of this factor on surface density conflicts with Larson’s velocity scaling relationship and the universality of turbulence within molecular clouds. However, this dependence is consistent with the prediction of Mouschovias (1987) that attributes the observed motions to Alfvén waves and the support of GMCs by the interstellar magnetic field.

This work was supported by NSF grant AST 0540852 and 0838222 to the Five College Radio Astronomy Observatory. The authors acknowledge valuable discussions with Telemachos Mouschovias and critical comments by the referee. We also thank Alberto Bolatto for providing the table of extragalactic GMC properties prior to publication. Finally, while this study challenges the results in SRBY, we acknowledge the many insightful contributions to studies of the molecular interstellar medium and star formation made by Phil Solomon, who passed away in 2008.

REFERENCES

- Arons, J., & Max, C. E. 1975, *ApJ*, 196, L77
Bloemen, J. B. G. M., et al. 1986, *A&A*, 154, 25
Bolatto, A. D., Leroy, A. K., Rosolowsky, E., Walter, F., & Blitz, L. 2008, *ApJ*, 686, 948
Brunt, C. M. 2003, *ApJ*, 584, 293
Clemens, D. P. 1985, *ApJ*, 295, 422
Dickman, R. L. 1978, *ApJS*, 37, 407
Elmegreen, B. G. 1989, *ApJ*, 338, 178
Freking, M. A., Langer, W. D., & Wilson, R. W. 1982, *ApJ*, 262, 590
Goldsmith, P. F., Heyer, M. H., Narayanan, G., Snell, R. L., Li, D., & Brunt, C. 2008, *ApJ*, 680, 428
Goodman, A. A., Barranco, J. A., Wilner, D. J., & Heyer, M. H. 1998, *ApJ*, 680, 428
Goodman, A. A., Pineda, J. E., & Schnee, S. L. 2008, arXiv:0806.3441
Heyer, M. H., & Brunt, C. M. 2004, *ApJ*, 615, L45
Heyer, M. H., Carpenter, J. M., & Snell, R. L. 2001, *ApJ*, 551, 852
Heyer, M. H., Williams, J. P., & Brunt, C. M. 2006, *ApJ*, 643, 956
Jackson, J. M., et al. 2006, *ApJS*, 163, 145
Lacy, J. H., Knacke, R., Geballe, T. R., & Tokunaga, A. T. 1994, *ApJ*, 428, L69
Larson, R. B. 1981, *MNRAS*, 194, 809
Liszt, H. S. 2007, *A&A*, 476, 291
McKee, C. F. 1989, *ApJ*, 345, 782
McKee, C. F., & Ostriker, E. C. 2007, *ARA&A*, 45, 565
Milam, S. N., Savage, C., Brewster, M. A., Ziurys, L. M., & Wyckoff, S. 2005, *ApJ*, 634, 1126
Mouschovias, T. Ch. 1987, in *Physical Processes in Interstellar Clouds*, ed. G. E. Morfill & M. Scholer (Dordrecht: Reidel), 453
Mouschovias, T. Ch., & Psaltis, D. 1995, *ApJ*, 444, L105
Mouschovias, T. Ch., Tassis, K., & Kunz, M. W. 2006, *ApJ*, 646, 1043
Myers, P. C., & Goodman, A. A. 1988a, *ApJ*, 329, 392
Myers, P. C., & Goodman, A. A. 1988b, *ApJ*, 326, L27
Penzias, A. A. 1980, *Science*, 208, 663
Pineda, J. E., Caselli, P., & Goodman, A. A. 2008, *ApJ*, 679, 481
Rohlfs, K., & Wilson, T. L. 2003, *Tools of Radio Astronomy* (Berlin: Springer)
Sanders, D. B., Clemens, D. P., Scoville, N. Z., & Solomon, P. M. 1986, *ApJS*, 60, 1
Solomon, P. M., & Rivolo, A. R. 1989, *ApJ*, 339, 919
Solomon, P. M., Rivolo, A. R., Barrett, J., & Yahil, A. (SRBY) 1987, *ApJ*, 319, 730
Strong, A. W., & Mattox, J. R. 1996, *A&A*, 308, L21
van Dishoeck, E. F., & Black, J. H. 1988, *ApJ*, 334, 771